Comput Mech (2011) 48:515–528
DOI 10.1007/s00466-011-0605-6

ORIGINAL PAPER

Fundamental-solution-based hybrid FEM for plane elasticity with special elements

Hui Wang · Qing-Hua Qin

Received: 23 November 2009 / Accepted: 26 April 2011 / Published online: 12 May 2011

Abstract The present paper develops a new type of hybrid finite element model with regular and special fundamental solutions (also known as Green's functions) as internal interpolation functions for analyzing plane elastic problems in structures weakened by circular holes. A variational functional used in the proposed model is first constructed, and then, the assumed intra-element displacement fields satisfying a priori the governing partial differential equations of the problem under consideration is constructed using a linear combination of fundamental solutions at a number of source points outside the element domain, as was done in the method of fundamental solutions. To ensure continuity of fields over inter-element boundaries, conventional shape functions are employed to construct the independent element frame displacement fields defined over the element boundary. The linkage of these two independent fields and the element stiffness equations in terms of nodal displacements are enforced by the minimization of the proposed variational functional. Special-purpose Green's functions associated with circular holes are used to construct a special circular hole element to effectively handle stress concentration problems without complicated local mesh refinement or mesh regeneration around the hole. The practical efficiency of the proposed element model is assessed via several numerical examples.

H. Wang
Institute of Scientific and Engineering Computation,
Henan University of Technology,
Zhengzhou 450052, China

H. Wang · Q.-H. Qin (✉)
Research School of Engineering, Australian National University,
Canberra, ACT 0200, Australia
e-mail: qinghua.qin@anu.edu.au

Keywords Boundary integral · Fundamental solutions · Hybrid finite element · Special circular hole element · Plane elasticity

1 Introduction

In the context of hybrid stress equilibrium finite elements, in which the equilibrating stresses with undetermined parameters in the element domain and the boundary displacements in terms of nodal displacements are independently approximated, pioneering applications are proposed by Pian [1]. As a variant of the hybrid stress equilibrium finite element methods, the hybrid Trefftz finite element method (HT-FEM) has been established by further constraining the stress basis to be associated with the satisfaction of all the governing equations of the problem in the element domain and has proved to be an efficient computational tool for solving engineering problems with local effects due to loading and/or geometry without troublesome mesh adjustment [2–4]. In the past decades, the HT-FEM has been successfully applied to problems of elasticity [5–7], plate bending [8,9], elastodynamic problems [10,11], transient heat conduction analysis [12], geometrically nonlinear plates [13], elasto-plasticity [14,15], piezoelectric materials [16], and nonlinear minimal surface problems [17]. Unlike the conventional finite element method (FEM) and boundary element method (BEM), the hybrid Trefftz FEM is based on a hybrid model which includes the use of independent auxiliary inter-element frame fields defined on each element boundary and independent intra-element fields chosen so as to a priori satisfy the homogeneous governing differential equations by means of a suitably truncated T-complete function set of homogeneous solutions. Inter-element continuity is enforced by using a modified variational principle, which is used to construct the

standard sparse symmetric force-displacement relationship, that is, the stiffness equation, and to establish a linkage between frame fields and internal fields of the element under consideration. The property of nonsingular element boundary integrals appearing in the hybrid Trefftz FEM enables us to conveniently construct arbitrarily shaped elements and special elements to effectively handle local effects, such as the elliptic hole element [4]. However, the general and special T-complete functions required by the HT-FEM may be difficult to generate for some physical problems.

As an alternative to the HT-FEM, a hybrid finite element formulation based on the fundamental solutions, called the HFS-FEM, was recently developed for solving two-dimensional linear or nonlinear thermal problems [18,19] and orthotropic elastic problems [20], which inherits the advantages of the HT-FEM over the FEM and the BEM, such as the possibility of high accuracy using coarse meshes of high-degree elements, enhanced insensitivity to mesh distortion, great liberty in element shape, possibility of accurately representing various local effects without troublesome mesh adjustment, etc, and avoids some disadvantages of the HT-FEM. In the HFS-FEM, the used fundamental solutions, instead of T-complete functions, also exactly satisfy a priori the governing partial differential equations for the problem under consideration. Due to this property of fundamental solutions, they are used to interpolate the element internal displacement fields with suitable combination and thus to transfer the element domain integral to the element boundary integrals in the modified hybrid variational functional using two independent variables, i.e. displacements on the element boundary and inside the element. The resulting system of equations is written in terms of nodal displacements only with symmetric stiffness matrix, which is easy to implement into the standard FEM. Compared to the HT-FEM, the proposed HFS-FEM has simpler interpolation kernel expressions and avoids the coordinate transformation procedure required in the HT-FEM to keep the matrix inversion stable, due to the usage of fundamental solutions. With the objective of making the computation more effective and making the meshing simpler around holes or other local defects, this paper derives the hybrid finite element formulation with general or special fundamental solutions kernels for plane elastic problems based on the variational principle presented in [18–20] and develops the concept of a special-purpose element. In particular, a special circular hole element is constructed to effectively handle the stress concentration around the hole boundary with reduced mesh refinement and regeneration effort.

The paper begins with a brief review of the basic equations of a plane elastic problem in Sect. 2 and the related fundamental solutions in Sect. 3. Then, a detailed derivation of the proposed HFS-FEM for plane elasticity and the corresponding algorithm is given in Sect. 4. Several numerical examples are presented in Sect. 5 to assess the efficiency of the proposed element model and some concluding remarks are provided in Sect. 6.

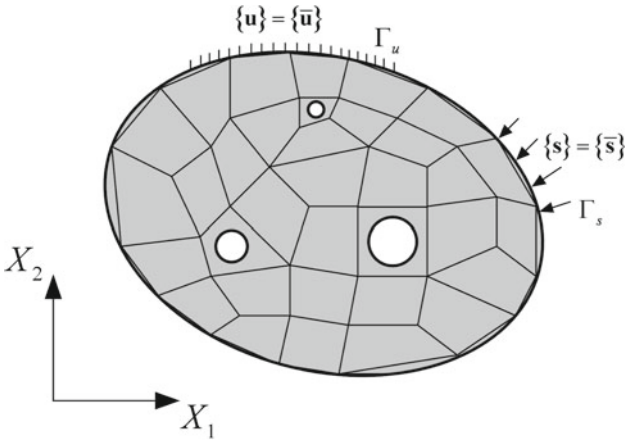

Fig. 1 Schematic diagram of plane elastic problem with circular cutouts and mesh used in the HFS-FEM

2 Basic equations for plane elasticity

For a well-posed plane elastic problem with circular cutouts in an arbitrary domain Ω, as shown in Fig. 1, the corresponding partial differential governing equations under the assumption of small deformation are given in matrix form as

$$\left.\begin{array}{l}[\mathbf{L}]\{\boldsymbol{\sigma}\}+\{\bar{\mathbf{b}}\}=\{\mathbf{0}\}\\ \{\boldsymbol{\varepsilon}\}=[\mathbf{L}]^{\mathrm{T}}\{\mathbf{u}\}\\ \{\boldsymbol{\sigma}\}=[\mathbf{D}]\{\boldsymbol{\varepsilon}\}\end{array}\right\}\ \text{in } \Omega \tag{1}$$

where $\{\boldsymbol{\sigma}\}=\{\sigma_{11}\ \ \sigma_{22}\ \ \sigma_{12}\}^{\mathrm{T}}$ and $\{\boldsymbol{\varepsilon}\}=\{\varepsilon_{11}\ \ \varepsilon_{22}\ \ \gamma_{12}\}^{\mathrm{T}}$ denote stress and strain vectors, respectively, $\{\bar{\mathbf{b}}\}=\{\bar{b}_1\ \ \bar{b}_2\}^{\mathrm{T}}$ body force vector, $\{\mathbf{u}\}=\{u_1\ \ u_2\}^{\mathrm{T}}$ displacement vector, and

$$\mathbf{L}=\begin{bmatrix}\partial_{,1} & 0 & \partial_{,2}\\ 0 & \partial_{,2} & \partial_{,1}\end{bmatrix} \tag{2}$$

the differential matrix, in which a comma denotes partial differentiation, i.e. $\partial_{,i}=\partial/\partial X_i$, and $X_i\,(i=1,2)$ are the global Cartesian coordinates. The stress-strain matrix is given by

$$\mathbf{D}=\frac{E^*}{1-\nu^{*2}}\begin{bmatrix}1 & \nu^* & 0\\ \nu^* & 1 & 0\\ 0 & 0 & \frac{1-\nu^*}{2}\end{bmatrix} \tag{3}$$

with $E^*=E$, $\nu^*=\nu$ for a plane stress problem and $E^*=E/(1-\nu^2)$, $\nu^*=\nu/(1-\nu)$ for a plane strain problem. E and ν denote respectively the elastic modulus and the Poisson's ratio.

Besides, following boundary displacement and traction conditions should be complemented to keep the system complete

$$\left.\begin{array}{ll}\{\mathbf{u}\}=\{\bar{\mathbf{u}}\} & \text{on } \Gamma_u\\ \{\mathbf{s}\}=[\mathbf{A}]\{\boldsymbol{\sigma}\}=\{\bar{\mathbf{s}}\} & \text{on } \Gamma_s\end{array}\right\} \tag{4}$$

where the overbar represents a given value, and

$$[\mathbf{A}] = \begin{bmatrix} n_1 & 0 & n_2 \\ 0 & n_2 & n_1 \end{bmatrix}, \quad \{\mathbf{s}\} = \begin{Bmatrix} s_1 & s_2 \end{Bmatrix}^{\mathrm{T}} \tag{5}$$

with n_i representing the ith component of the unit outward normal to the boundary $\Gamma = \Gamma_u + \Gamma_s$.

Rearranging Eq. (1) leads to the following Cauchy-Navier equations in terms of displacements

$$[\mathbf{L}]\,[\mathbf{D}]\,[\mathbf{L}]^{\mathrm{T}}\,\{\mathbf{u}\} + \left\{\bar{\mathbf{b}}\right\} = \{\mathbf{0}\} \tag{6}$$

3 Fundamental solutions

For plane elastic problems involving holes, it is convenient to express the fundamental solutions in terms of complex variables. In plane elastic theory, all components of elastic fields including the stresses $\sigma_{11}, \sigma_{22}, \sigma_{12}$, the displacements u_1, u_2 and the resultant forces P_1, P_2 along a curve can be expressed in terms of two complex analytic functions $\phi(z)$ and $\psi(z)$ [21] as

$$\begin{cases} 2G(u_1 + u_2\mathrm{I}) = \kappa\phi(z) - z\overline{\phi'(z)} - \overline{\psi(z)} \\ \sigma_{11} + \sigma_{22} = 4\mathrm{Re}\left[\phi'(z)\right] \\ \sigma_{22} - \sigma_{11} + 2\sigma_{12}\mathrm{I} = 2\left\{\bar{z}\phi''(z) + \psi'(z)\right\} \\ P_1 + P_2\mathrm{I} = 2\mathrm{I}\left\{\phi(z) + z\overline{\phi'(z)} + \overline{\psi(z)}\right\} \end{cases} \tag{7}$$

where $G = E/2/(1+\nu), \kappa = (3-\nu)/(1+\nu)$ for plane stress and $\kappa = 3 - 4\nu$ for plane strain, $z = x_1 + x_2\mathrm{I}$ is the complex coordinate in the z-plane with $\mathrm{I} = \sqrt{-1}$, the overbar denotes complex conjugation, Re denotes the real part of the function and prime denotes differentiation with respect to the argument z.

3.1 A point force in an infinite plane

If a concentrated force $F = F_1 + F_2\mathrm{I}$ is located at the point $z_0 = x_1^s + x_2^s\mathrm{I}$ in the infinite plane, the complex functions can be written as [21]

$$\begin{cases} \phi(z) = M\ln(z - z_0) \\ \psi(z) = N\ln(z - z_0) - M\frac{\bar{z}_0}{z - z_0} \end{cases} \tag{8}$$

where

$$M = -\frac{F}{2\pi(1+\kappa)}, N = -\kappa\bar{M}$$

Obviously, the complex functions in Eq. (8) are singular at the point z_0, which can be taken as the basis for constructing more complex fundamental solutions.

By substituting Eq. (8) into Eq. (7), the classical formation of the Kelvin solution can be obtained. For example, for plane strain problems, if $u_{li}^*(z, z_0)$ and $\sigma_{lij}^*(z, z_0)$ are the induced displacements and stresses at z due to l-direction unit force at z_0, we have [22]

$$\begin{aligned} u_{li}^* &= \frac{1}{8\pi G(1-\nu)}\left[(3-4\nu)\,\delta_{li}\ln\frac{1}{r} + r_{,l}r_{,i}\right] \\ \sigma_{lij}^* &= \frac{1}{4\pi\,(1-\nu)\,r}\left[(1-2\nu)\left(r_{,l}\delta_{ij} - r_{,j}\delta_{il} - r_{,i}\delta_{jl}\right)\right. \\ &\qquad \left. - 2r_{,i}r_{,j}r_{,l}\right] \end{aligned} \tag{9}$$

where r stands for the distance between z and z_0.

3.2 A point force in an infinite plane with circular hole

Consider a point force $F = F_1 + F_2\mathrm{I}$ at z_0 in an infinite plane with a centered circular hole of radius a. Using the complex variable formalism above, the fundamental solution sought can be expressed in the form

$$\begin{cases} \phi(z) = \phi_s(z) + \phi_r(z) \\ \psi(z) = \psi_s(z) + \psi_r(z) \end{cases} \tag{10}$$

where ϕ_s and ψ_s are the singular terms for the infinite homogeneous body, which is the Kelvin's solution expressed in terms of complex variable listed above, and ϕ_r and ψ_r are regular terms to be determined so that the resultant tractions on the surface of the circular hole become zero. Furthermore, the vanishing stress conditions at infinity should also be satisfied.

Using the analytical continuation approach, the regular terms (also called imaging terms) can be obtained as [23]

$$\begin{cases} \phi_r(z, z_0^*) = -z\overline{\phi_s'(z^*, z_0)} - \overline{\psi_s(z^*, z_0)} \\ \psi_r(z, z_0^*) = -\overline{\phi_s(z^*, z_0)} - \overline{z^*\phi_r'(z, z_0^*)} \end{cases} \tag{11}$$

where $z^* = a^2/\bar{z}, z_0^* = a^2/\bar{z}_0$.

Substituting the known singular terms and retaining the main parts of Eq. (11) gives the following solutions:

$$\begin{cases} \phi_r(z, z_0) = -\bar{N}\ln\left(\frac{z - z_0^*}{z}\right) - \bar{M}\frac{z_0 - z_0^*}{z - z_0^*}\frac{z_0^*}{\bar{z}_0} \\ \psi_r(z, z_0) = -\bar{M}\ln\left(\frac{z - z_0^*}{z}\right) + \bar{N}\frac{a^2}{z - z_0^*}\frac{1}{z} - \bar{N}\frac{a^2}{z^2} \\ \qquad\qquad -\bar{M}\frac{z_0^{*2}(z_0 - z_0^*)}{z(z - z_0^*)^2} + M\frac{\overline{z_0^*}}{z} \end{cases} \tag{12}$$

Having determined the two complex functions, the related displacement and stress solutions can be obtained using Eq. (7).

4 Development of HFS finite element formulation

In this section, the procedure for developing a hybrid finite element model with the fundamental solutions as the interior trial functions is described for solving the boundary value problem (BVP) defined by Eqs. (1), (4) and (13) below.

As in the hybrid Trefftz FEM, the main aim of the proposed approach is to establish a hybrid finite element formulation whereby intra-element continuity is enforced on

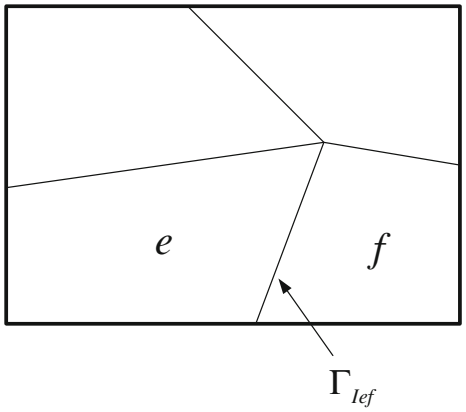

Fig. 2 Illustration of continuity between two adjacent elements 'e' and 'f'

nonconforming internal displacement fields formed by a linear combination of fundamental solutions at source points outside the element domain under consideration, while auxiliary frame displacement fields are independently defined on the element boundary to enforce field continuity across inter-element boundaries. But unlike the hybrid Trefftz FEM, the intra-element fields in the HFS-FEM are constructed based on the fundamental solutions, rather than a truncated T-complete function set. Subsequently, a variational functional associated with the new displacement trial functions inside the element and displacements on the element boundary is required to generate the related stiffness matrix equation. As the solution domain is divided into a number of elements denoted by Ω_e with the element boundary Γ_e, the following inter-element continuity related to displacements and tractions is usually required on the common boundary Γ_{Ief} between any two adjacent elements 'e' and 'f' (see Fig. 2):

$$\left.\begin{array}{l}\{\mathbf{u}_e\} = \{\mathbf{u}_f\} \\ \{\mathbf{s}_e\} + \{\mathbf{s}_f\} = \{\mathbf{0}\}\end{array}\right\} \text{ on } \Gamma_e \cap \Gamma_f \tag{13}$$

in the proposed hybrid FE approach.

4.1 Non-conforming intra-element fields

In the absence of body forces, and motivated by the method of fundamental solution (MFS) [24] to remove the singularity of the fundamental solution, for a particular element shown in Fig. 3, say element e, which occupies the subdomain Ω_e, we first assume that the field variable defined in the element domain is approximated by a linear combination of fundamental solutions centered at different source points (see Fig. 3) as

$$\begin{aligned}\{\mathbf{u}_e\} &= \sum_{j=1}^{n_s} \begin{bmatrix} u_{11}^*(\mathbf{x},\mathbf{y}_j) & u_{21}^*(\mathbf{x},\mathbf{y}_j) \\ u_{12}^*(\mathbf{x},\mathbf{y}_j) & u_{22}^*(\mathbf{x},\mathbf{y}_j)\end{bmatrix} \begin{Bmatrix} c_{1j} \\ c_{2j}\end{Bmatrix} \\ &= [\mathbf{N}]\{\mathbf{c}_e\} \ (\forall \mathbf{x} \in \Omega_e, \mathbf{y}_j \notin \Omega_e)\end{aligned} \tag{14}$$

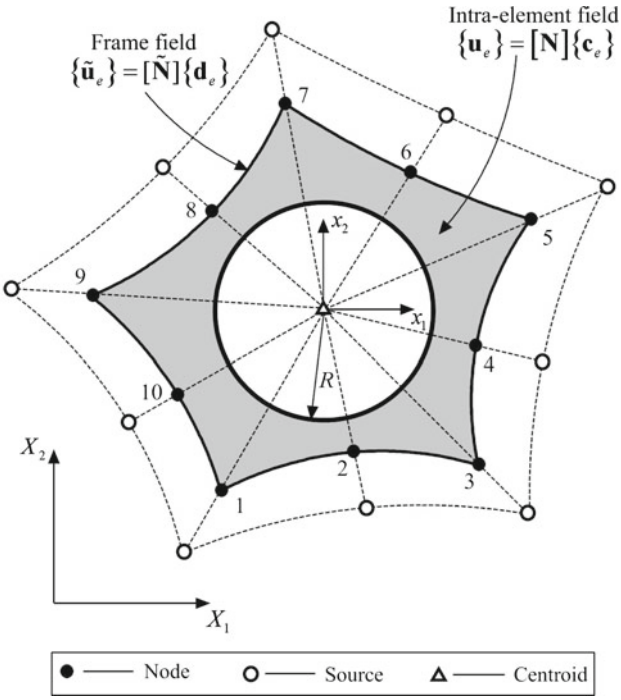

Fig. 3 Intra-element fields and frame fields in a particular element in the HFS-FEM

where n_s is the number of virtual sources outside the element domain, $\{\mathbf{c}_e\} = \begin{bmatrix} c_{11} & c_{21} & \cdots & c_{1n_s} & c_{2n_s}\end{bmatrix}^{\mathrm{T}}$ is an unknown coefficient vector (not nodal displacements), and the coefficient matrix

$$[\mathbf{N}] = \begin{bmatrix} u_{11}^*(\mathbf{x},\mathbf{y}_1) & u_{21}^*(\mathbf{x},\mathbf{y}_1) & | \cdots | & u_{11}^*(\mathbf{x},\mathbf{y}_{n_s}) & u_{21}^*(\mathbf{x},\mathbf{y}_{n_s}) \\ & & | \quad | & & \\ u_{12}^*(\mathbf{x},\mathbf{y}_1) & u_{22}^*(\mathbf{x},\mathbf{y}_1) & | \cdots | & u_{12}^*(\mathbf{x},\mathbf{y}_{n_s}) & u_{22}^*(\mathbf{x},\mathbf{y}_{n_s})\end{bmatrix}$$

where $\mathbf{x}$ and $\mathbf{y}_i$ are the field point and source point defined in the local coordinate system (x_1, x_2), respectively.

In practice, the generation of virtual sources outside the element domain can be placed on the so-called pseudo-boundary similar to the physical boundary of the element and can usually be given by means of the formulation [18–20,25,26]

$$\mathbf{y} = \mathbf{x}_b + \gamma\,(\mathbf{x}_b - \mathbf{x}_c) \tag{15}$$

where γ is a dimensionless coefficient, $\mathbf{x}_b$ is the elementary boundary point and $\mathbf{x}_c$ the geometrical centroid of the element. Typically, for simplicity in the proposed approach we use the nodes of the element to generate related source points.

Similar to the procedure in the MFS, the theoretical determination of the locations of sources in the proposed HFS-FEM is an open question. However, numerical experiments show that there is a large interval to select the suitable value of γ, by which satisfying accuracy and stability can be achieved [18–20]. In this paper, similar numerical tests in the context of plane elasticity is performed to illustrate this issue.

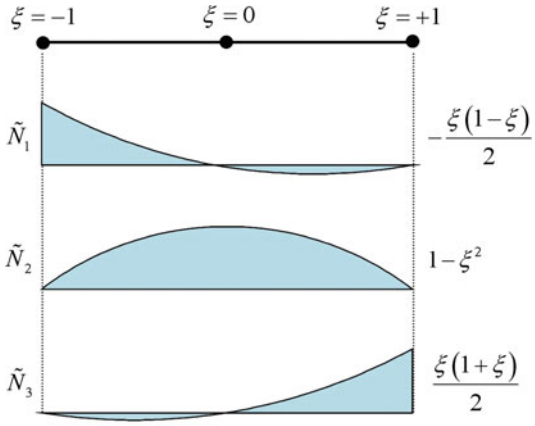

Fig. 4 Typical quadratic interpolation for the frame fields

Subsequently, differentiating Eq. (14) and substituting it into Eq. (1) yields the corresponding stress fields

$$\{\boldsymbol{\sigma}_e\} = [\mathbf{T}]\{\mathbf{c}_e\} \tag{16}$$

with

$$[\mathbf{T}] = \begin{bmatrix} \sigma^*_{111}(\mathbf{x},\mathbf{y}_1)\ \sigma^*_{211}(\mathbf{x},\mathbf{y}_1) & |\cdots| & \sigma^*_{111}(\mathbf{x},\mathbf{y}_{n_s})\ \sigma^*_{211}(\mathbf{x},\mathbf{y}_{n_s}) \\ \sigma^*_{122}(\mathbf{x},\mathbf{y}_1)\ \sigma^*_{222}(\mathbf{x},\mathbf{y}_1) & |\cdots| & \sigma^*_{122}(\mathbf{x},\mathbf{y}_{n_s})\ \sigma^*_{222}(\mathbf{x},\mathbf{y}_{n_s}) \\ \sigma^*_{112}(\mathbf{x},\mathbf{y}_1)\ \sigma^*_{212}(\mathbf{x},\mathbf{y}_1) & |\cdots| & \sigma^*_{112}(\mathbf{x},\mathbf{y}_{n_s})\ \sigma^*_{212}(\mathbf{x},\mathbf{y}_{n_s}) \end{bmatrix}$$

Furthermore, the element boundary traction vector $\{\mathbf{s}_e\}$ is evaluated by

$$\{\mathbf{s}_e\} = [\mathbf{Q}]\{\mathbf{c}_e\} \tag{17}$$

where $[\mathbf{Q}] = [\mathbf{A}][\mathbf{T}]$.

4.2 Auxiliary conforming frame fields

In order to enforce conformity on the displacement vector $\{\mathbf{u}\}$ along the inter-element boundary, for instance $\{\mathbf{u}_e\} = \{\mathbf{u}_f\}$ on $\Gamma_e \cap \Gamma_f$, of any two neighboring elements e and f, auxiliary inter-element frame fields $\{\tilde{\mathbf{u}}_e\}$ are assumed in terms of the nodal degrees of freedom (DOF), $\{\mathbf{d}_e\}$, as used in the conventional FEM. For example, for the element shown in Fig. 3 containing 10 nodes, the frame fields $\{\tilde{\mathbf{u}}_e\}$ over the second edge consisting of nodes 3, 4, and 5 are written as

$$\{\tilde{\mathbf{u}}_e\} = [\tilde{\mathbf{N}}]\{\mathbf{d}_e\} \tag{18}$$

in which the shape function matrix $[\tilde{\mathbf{N}}]$ and the nodal vector $\{\mathbf{d}_e\}$ are given by

$$[\tilde{\mathbf{N}}] = \begin{bmatrix} 0\ 0\ |\cdots|\ \tilde{N}_1\ \ 0\ \ |\tilde{N}_2\ \ 0|\ \ \tilde{N}_3\ \ 0\ \ |\cdots|\ 0\ 0 \\ 0\ 0\ |\cdots|\ \ 0\ \ \tilde{N}_1\ \ |0\ \ \tilde{N}_2|\ \ 0\ \ \tilde{N}_3\ |\cdots|\ 0\ 0 \end{bmatrix}$$

$$\{\mathbf{d}_e\} = \left\{u_1^1\ u_2^1\ |\cdots|\ u_1^3\ u_2^3|\ u_1^4\ u_2^4|\ u_1^5\ u_2^5|\cdots|\ u_1^{10}\ u_2^{10}\right\}^{\mathrm{T}}$$

and $\tilde{N}_i$ $(i = 1, 2, 3)$ stands for shape functions in terms of the natural coordinate ξ defined in Fig. 4, u_i^k $(i = 1, 2)$ denotes the nodal displacement at nodal k.

4.3 Variational principle and stiffness equation

4.3.1 Variational functional

For the boundary value problem defined in Eqs. (1)–(4) and 13, since the stationary conditions of the traditional potential or complementary variational functional cannot guarantee satisfaction of the inter-element continuity conditions required in the proposed model, a modified variational functional based on two independent displacement fields is defined as follows:

$$\Pi_m = \sum_e \Pi_{me} = \sum_e \left[\int_{\Omega_e} U_\varepsilon \mathrm{d}\Omega - \int_{\Omega_e} \bar{b}_i u_i \mathrm{d}\Omega - \int_{\Gamma_e^s} \bar{s}_i \tilde{u}_i \mathrm{d}\Gamma + \int_{\Gamma_e} s_i\,(\tilde{u}_i - u_i)\,\mathrm{d}\Gamma \right] \tag{19}$$

where U_ε is the strain energy density defined as

$$U_\varepsilon = \frac{1}{2}\sigma_{ij}\varepsilon_{ij} \tag{20}$$

In Eq. (19), the governing Equation 6 holds true, a priori, within the element domain due to the use of the fundamental solutions as intra-element trial functions, and the boundary displacement satisfies the essential boundary conditions. It should be mentioned that the variational functional (19) is different from that used in Refs [2,27] in which three independent variables are used. The similar principle to construct variational functional with two independent variables can be found for potential problems [18,19,28]. The boundary Γ_e of a particular element e consists of the following parts

$$\Gamma_e = \Gamma_e^u \cup \Gamma_e^s \cup \Gamma_e^I \tag{21}$$

where $\Gamma_e^u = \Gamma_e \cap \Gamma_u$, $\Gamma_e^s = \Gamma_e \cap \Gamma_s$ and Γ_e^I stands for the inter-element boundary of the element 'e'.

4.3.1.1 Stationary condition of the proposed variational functional

Next we will show that the stationary condition of the functional (19) leads to the governing Eq. (1), boundary conditions (4), and continuity conditions (13). For this purpose, the first-order variational of Eq. (19) yields

$$\delta\Pi_{me} = \int_{\Omega_e} \delta U_\varepsilon \mathrm{d}\Omega - \int_{\Omega_e} \bar{b}_i \delta u_i \mathrm{d}\Omega - \int_{\Gamma_e^s} \bar{s}_i \delta\tilde{u}_i \mathrm{d}\Gamma + \int_{\Gamma_e} \delta s_i\,(\tilde{u}_i - u_i)\,\mathrm{d}\Gamma + \int_{\Gamma_e} s_i\,(\delta\tilde{u}_i - \delta u_i)\,\mathrm{d}\Gamma \tag{22}$$

in which the first term is given as

$$\int_{\Omega_e} \delta U_\varepsilon \mathrm{d}\Omega = \int_{\Omega_e} \sigma_{ij}\delta\varepsilon_{ij}\mathrm{d}\Omega = \int_{\Omega_e} \sigma_{ij}\delta u_{i,j}\mathrm{d}\Omega \tag{23}$$

Using the Gaussian theorem

$$\int_{\Omega} f_{,i}\mathrm{d}\Omega = \int_{\Gamma} f n_i \mathrm{d}\Gamma \tag{24}$$

we have

$$\int_{\Omega_e} \delta U_\varepsilon \mathrm{d}\Omega = \int_{\Gamma_e} s_i \delta u_i \mathrm{d}\Gamma - \int_{\Omega_e} \sigma_{ij,j}\delta u_i \mathrm{d}\Omega \tag{25}$$

Then, substituting Eq. (25) into Eq. (22) gives

$$\begin{aligned}\delta\Pi_{me} = &-\int_{\Omega_e} \left(\sigma_{ij,j} + \bar{b}_i\right)\delta u_i \mathrm{d}\Omega - \int_{\Gamma_e^s} \bar{s}_i \delta\tilde{u}_i \mathrm{d}\Gamma \\ &+ \int_{\Gamma_e} \delta s_i \left(\tilde{u}_i - u_i\right)\mathrm{d}\Gamma + \int_{\Gamma_e} s_i \delta\tilde{u}_i \mathrm{d}\Gamma\end{aligned} \tag{26}$$

For the stress-based method, the displacement conformity is satisfied in advance, that is,

$$\begin{aligned}&\delta\tilde{u}_i = 0 \quad \text{on } \Gamma_e^u \quad (\because \tilde{u}_i = \bar{u}_i) \\ &\delta\tilde{u}_i^e = \delta\tilde{u}_i^f \quad \text{on } \Gamma_{ef}^I \quad (\because \tilde{u}_i^e = \tilde{u}_i^f)\end{aligned} \tag{27}$$

then, Eq. (26) can be rewritten as

$$\begin{aligned}\delta\Pi_{me} = &-\int_{\Omega_e} \left(\sigma_{ij,j} + \bar{b}_i\right)\delta u_i \mathrm{d}\Omega + \int_{\Gamma_e^s} (s_i - \bar{s}_i)\,\delta\tilde{u}_i \mathrm{d}\Gamma \\ &+ \int_{\Gamma_e^I} s_i \delta\tilde{u}_i \mathrm{d}\Gamma + \int_{\Gamma_e} \delta s_i \left(\tilde{u}_i - u_i\right)\mathrm{d}\Gamma\end{aligned} \tag{28}$$

from which the governing equation in the domain Ω_e and boundary conditions on Γ_e^s can be obtained

$$\begin{aligned}&\sigma_{ij,j} + \bar{b}_i = 0 \qquad \text{in } \Omega_e \\ &s_i = \sigma_{ij} n_j = \bar{s}_i \qquad \text{on } \Gamma_e^s \\ &\tilde{u}_i = u_i \qquad \text{on } \Gamma_e^u\end{aligned} \tag{29}$$

by using the stationary condition $\delta\Pi_{me} = 0$ and the arbitrariness of quantities δu_i, $\delta\tilde{u}_i$ and δs_i.

As to the continuity requirement between the two adjacent elements 'e' and 'f' given in Eq. (13), we can obtain it in the following way. When assembling elements 'e' and 'f', we have

$$\begin{aligned}\delta\Pi_{m(e+f)} = &-\int_{\Omega_e+\Omega_f} \left(\sigma_{ij,j} + \bar{b}_i\right)\delta u_i \mathrm{d}\Omega \\ &+ \int_{\Gamma_e^s+\Gamma_f^s} (s_i - \bar{s}_i)\,\delta\tilde{u}_i \mathrm{d}\Gamma \\ &+ \int_{\Gamma_{ef}^I} \left(s_{ie} + s_{if}\right)\delta\tilde{u}_i \mathrm{d}\Gamma + \int_{\Gamma_e+\Gamma_f} \delta s_i \left(\tilde{u}_i - u_i\right)\mathrm{d}\Gamma\end{aligned} \tag{30}$$

from which the vanishing variation of $\Pi_{m(e+f)}$leads to the continuity condition $s_{ie} + s_{if} = 0$ on the inter-element boundary Γ_{ef}^I.

4.3.1.2 Theorem on the existence of extremum

If the expression

$$\int_{\Omega} \delta^2 U_\varepsilon \mathrm{d}\Omega - \sum_e \left[\int_{\Gamma_e} \delta s_{ie}(\delta\tilde{u}_{ie} - \delta u_{ie})\mathrm{d}\Gamma + \int_{\Gamma_e^I} \delta s_{ie}\delta\tilde{u}_{ie}\mathrm{d}\Gamma\right] \tag{31}$$

is uniformly positive (or negative) in the neighborhood of u_{i0}, where the displacement u_{i0} has such a value that $\Pi_m(u_{i0}) = (\Pi_m)_0$, and where $(\Pi_m)_0$ stands for the stationary value of Π_m, we have

$$\Pi_m \geq (\Pi_m)_0 \,[\text{or } \Pi_m \leq (\Pi_m)_0] \tag{32}$$

in which the relation that $\tilde{u}_{ie} = \tilde{u}_{if}$ is identical on $\Gamma_e \cap \Gamma_f$ has been used. This is due to the definition in Eq. (13) of Sect. 4.

Proof The proof of the theorem on the existence of extremum may be completed by way of the so-called "second variational approach" [29]. In doing this, performing variation of $\delta\Pi_m$ and using the constrained conditions (1), we find

$$\begin{aligned}\delta^2\Pi_m = &\int_{\Omega} \delta^2 U_\varepsilon \mathrm{d}\Omega - \sum_e \left[\int_{\Gamma_e} \delta s_{ie}(\delta\tilde{u}_{ie} - \delta u_{ie})\mathrm{d}\Gamma \right. \\ &\left. + \int_{\Gamma_e^I} \delta s_{ie}\delta\tilde{u}_{ie}\mathrm{d}\Gamma\right] = \text{expression (31)}\end{aligned} \tag{33}$$

Therefore the theorem has been proved from the sufficient condition of the existence of a local extreme of a functional [29]. This completes the proof. □

4.3.2 Stiffness equation

Having independently defined the intra-element fields and frame fields in a particular element (see Fig. 3), the next

step is to generate the element stiffness equation from the proposed functional.

The functional Π_{me} corresponding to a particular element e of the present problem can be written as

$$\Pi_{me} = \frac{1}{2}\int_{\Omega_e} \sigma_{ij}\varepsilon_{ij}\mathrm{d}\Omega - \int_{\Omega_e} \bar{b}_i u_i \mathrm{d}\Omega - \int_{\Gamma_e^s} \bar{s}_i \tilde{u}_i \mathrm{d}\Gamma + \int_{\Gamma_e} s_i\left(\tilde{u}_i - u_i\right)\mathrm{d}\Gamma \tag{34}$$

Appling the Gaussian theorem again to the above functional and considering the equilibrium equation $\sigma_{ij,j} + \bar{b}_i = 0$, we have the final expression for the HFS finite element model

$$\Pi_{me} = -\frac{1}{2}\int_{\Gamma_e} s_i u_i \mathrm{d}\Gamma - \frac{1}{2}\int_{\Omega_e} \bar{b}_i u_i \mathrm{d}\Omega - \int_{\Gamma_e^s} \bar{s}_i \tilde{u}_i \mathrm{d}\Gamma + \int_{\Gamma_e} s_i \tilde{u}_i \mathrm{d}\Gamma \tag{35}$$

In the absence of body forces, substituting Eqs. (14), (17) and (18) into the functional (35) produces

$$\Pi_{me} = -\frac{1}{2}\{\mathbf{c}_e\}^{\mathrm{T}}[\mathbf{H}_e]\{\mathbf{c}_e\} - \{\mathbf{d}_e\}^{\mathrm{T}}\{\mathbf{g}_e\} + \{\mathbf{c}_e\}^{\mathrm{T}}[\mathbf{G}_e]\{\mathbf{d}_e\} \tag{36}$$

in which

$$\begin{aligned}
[\mathbf{H}_e] &= \int_{\Gamma_e} [\mathbf{Q}]^{\mathrm{T}}[\mathbf{N}]\mathrm{d}\Gamma \\
[\mathbf{G}_e] &= \int_{\Gamma_e} [\mathbf{Q}]^{\mathrm{T}}[\tilde{\mathbf{N}}]\mathrm{d}\Gamma \\
\{\mathbf{g}_e\} &= \int_{\Gamma_e^s} [\tilde{\mathbf{N}}]^{\mathrm{T}}\{\bar{\mathbf{s}}\}\mathrm{d}\Gamma
\end{aligned} \tag{37}$$

To enforce inter-element continuity on the common element boundary, the unknown vector $\{\mathbf{c}_e\}$ should be expressed in terms of nodal DOF $\{\mathbf{d}_e\}$. The minimization of the functional Π_{me} with respect to $\{\mathbf{c}_e\}$ and $\{\mathbf{d}_e\}$, respectively, yields

$$\begin{aligned}
\frac{\partial \Pi_{me}}{\partial \{\mathbf{c}_e\}^{\mathrm{T}}} &= -[\mathbf{H}_e]\{\mathbf{c}_e\} + [\mathbf{G}_e]\{\mathbf{d}_e\} = \mathbf{0} \\
\frac{\partial \Pi_{me}}{\partial \{\mathbf{d}_e\}^{\mathrm{T}}} &= [\mathbf{G}_e]^{\mathrm{T}}\{\mathbf{c}_e\} - \{\mathbf{g}_e\} = \mathbf{0}
\end{aligned} \tag{38}$$

from which the optional relationship between $\{\mathbf{c}_e\}$ and $\{\mathbf{d}_e\}$, and the stiffness equation can be produced

$$\begin{aligned}
\{\mathbf{c}_e\} &= [\mathbf{H}_e]^{-1}[\mathbf{G}_e]\{\mathbf{d}_e\} \\
[\mathbf{K}_e]\{\mathbf{d}_e\} &= \{\mathbf{g}_e\}
\end{aligned} \tag{39}$$

where $[\mathbf{K}_e] = [\mathbf{G}_e]^{\mathbf{T}}[\mathbf{H}_e]^{-1}[\mathbf{G}_e]$ stands for the element stiffness matrix, which is symmetric.

It is worth pointing out that the evaluation of right-handed vector $\{\mathbf{g}_e\}$ in Eq. (39) is the same as that in the conventional FEM, so it is convenient to incorporate the proposed HFS-FEM into the standard FEM program. Besides, the stress and traction estimations are directly computed from approximations (16) and (17), respectively. The boundary displacements, sufficient to draw the deflected shape of the structure, are computed directly from approximation (18). However, the displacements at interior points of the hybrid stress elements have to be determined from approximation (14) with recovered rigid-body modes in each element by post-processing operations as below.

4.4 Recovery of rigid-body motion

By checking the above procedure, we know that the solution fails if any of the functions u_{li}^* is in a rigid body motion mode. As a consequence, the matrix $[\mathbf{H}_e]$ is not in full rank and becomes singular for inversion. Therefore, special care should be taken to discard all rigid body motion terms from $\{\mathbf{u}_e\}$ to prevent the element deformability matrix $[\mathbf{H}_e]$ from being singular.

However, it is necessary to reintroduce the discarded rigid-body modes in the internal field $\{\mathbf{u}_e\}$ of a particular element and then to calculate corresponding rigid-body amplitude by requiring local or average fitting, for example, the least squares adjustment of $\{\mathbf{u}_e\}$ and $\{\tilde{\mathbf{u}}_e\}$. In this case, these missing terms can easily be recovered by setting for the augmented internal field [2,3,5]

$$\left\{\hat{\mathbf{u}}_e\right\} = \{\mathbf{u}_e\} + \begin{bmatrix} 1 & 0 & x_2 \\ 0 & 1 & -x_1 \end{bmatrix}\{\mathbf{c}_0\} \tag{40}$$

where the undetermined rigid-body amplitude vector $\{\mathbf{c}_0\}$ can be calculated using the least square matching of $\{\mathbf{u}_e\}$ and $\{\tilde{\mathbf{u}}_e\}$ at n element nodes

$$\sum_{i=1}^{n}\left[\left(u_1^i - \tilde{u}_1^i\right)^2 + \left(u_2^i - \tilde{u}_2^i\right)^2\right] = \min \tag{41}$$

which finally yields

$$[\mathbf{R}_e]\{\mathbf{c}_0\} = \{\mathbf{r}_e\} \tag{42}$$

with

$$[\mathbf{R}_e] = \sum_{i=1}^{n}\begin{bmatrix} 1 & 0 & x_{2i} \\ 0 & 1 & -x_{1i} \\ x_{2i} & -x_{1i} & x_{1i}^2 + x_{2i}^2 \end{bmatrix} \tag{43}$$

$$\{\mathbf{r}_e\} = \sum_{i=1}^{n}\begin{Bmatrix} d_{e1}^i - u_{e1}^i \\ d_{e2}^i - u_{e2}^i \\ \left(d_{e1}^i - u_{e1}^i\right)x_{2i} - \left(d_{e2}^i - u_{e2}^i\right)x_{1i} \end{Bmatrix} \tag{44}$$

As a result, once the nodal field $\{\mathbf{d}_e\}$ and the interpolation coefficient $\{\mathbf{c}_e\}$ are determined by solving Eqs. (39), then $\{\mathbf{c}_0\}$ can be evaluated from Eq. (42). Finally, the complete

displacement field $\{\hat{\mathbf{u}}_e\}$ at any interior point in a particular element can be obtained by means of Eq. (40).

5 Numerical assessment

A number of examples are presented to illustrate the effectiveness of the proposed method in this section. Firstly, the patch test is carried out, and then the accuracy and stability of the proposed numerical model are studied by considering uniform pressure applied to the internal boundary of a cylinder. Subsequently, we consider a bimaterial problem to investigate the effect of mesh distortion and show the feasibility of the proposed numerical method for treating multi-material problems, by comparison with other Green's-functions-based methods such as the MFS and the BEM. As the final example, an infinite plate with a circular hole subjected to remote tension is studied to demonstrate the appealing performance of the proposed special-purpose element model.

Besides, for the purpose of error estimation and convergence studies, the percentage relative error

$$\text{Rerr}(u) = \frac{|u^e - u^n|}{|u^e|} \times 100\% \tag{45}$$

and the normalized Euclid norm error

$$\text{Nerr}(u) = \frac{1}{N}\sqrt{\sum_{i=1}^{N}\left(u_i^e - u_i^n\right)^2} \tag{46}$$

are defined. In Eqs. (45) and (46), superscripts (e) and (n) refer to the exact and numerical solutions, respectively. N is the number of sample points.

5.1 Patch test

To conduct the patch test, a square of dimension $[0, 1]\times[0, 1]$ is considered and a known linear displacement profile [27]

$$u_1 = 2X_1 + 3X_2, \quad u_2 = 3X_1 + 2X_2 \tag{47}$$

is specified on all boundaries.

In the present calculation, the patch test is carried out for a plane strain state with $E = 2.5$ and $\nu = 0.25$. The square patch is modeled with one 8-node element and 5 random interior points and 9 uniformly spaced interior points are arranged in the domain. The displacements at the interior points and the boundary tractions are computed for the purpose of patch test. Table 1 lists the approximated displacements of the internal points and they are compared with the analytical solutions given by Eq. (47). It is observed that the linear field can be approximated by the superposition of finite number of the fundamental solutions with relatively high accuracy. Moreover, the computed tractions along the boundary and the related exact solutions are shown in Fig. 5, in which the horizontal axis denotes the length of the boundary starting from the origin and measuring in anti-clock direction. The figure shows that the results vary smoothly and agree with the exact solutions on the boundary. So it is very appealing that the patch test is passed successfully.

Table 1 Percentage relative errors at various internal points for the patch test

Coordinate	$\boldsymbol{Rerr}(u_1)(\times 10^{-3})$	$\boldsymbol{Rerr}(u_2)(\times 10^{-3})$
(0.3404, 0.5060)	0.0000	0.0000
(0.5853, 0.6991)	0.0000	0.0000
(0.2238, 0.8909)	6.4096	4.0763
(0.7513, 0.9593)	0.0000	2.3966
(0.2551, 0.5472)	0.0000	0.0000
(0.2500, 0.2500)	0.0000	0.0000
(0.2500, 0.5000)	0.0000	0.0000
(0.2500, 0.7500)	3.6364	4.4444
(0.5000, 0.2500)	0.0000	0.0000
(0.5000, 0.5000)	0.0000	0.0000
(0.5000, 0.7500)	0.0000	0.0000
(0.7500, 0.2500)	4.4444	3.6364
(0.7500, 0.5000)	0.0000	0.0000
(0.7500, 0.7500)	0.0000	0.0000

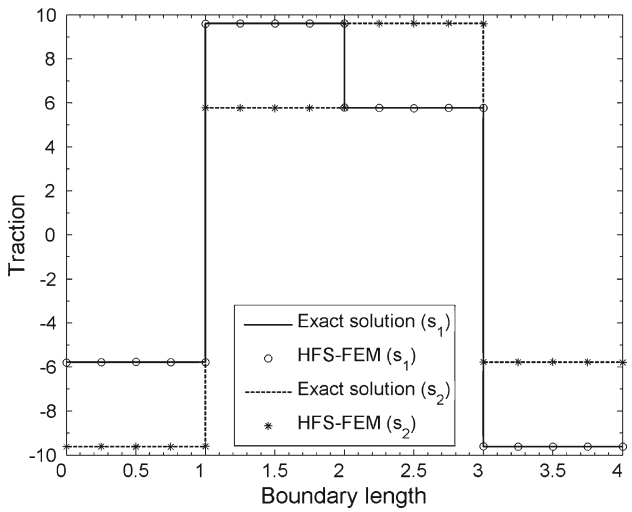

Fig. 5 Traction distributions over the square boundary for the patch test

5.2 Thick-walled cylinder under interior pressure

Consider a long, thick-walled cylinder with inner radius $r_i = 5$ and outer radius $r_o = 20$. Uniform pressure $p = 10$ is applied to the inner circular boundary. The elastic modulus E is assumed to be 1000, and the Poisson's ratio ν to be 0.3. The analytical solutions of the displacements and stresses

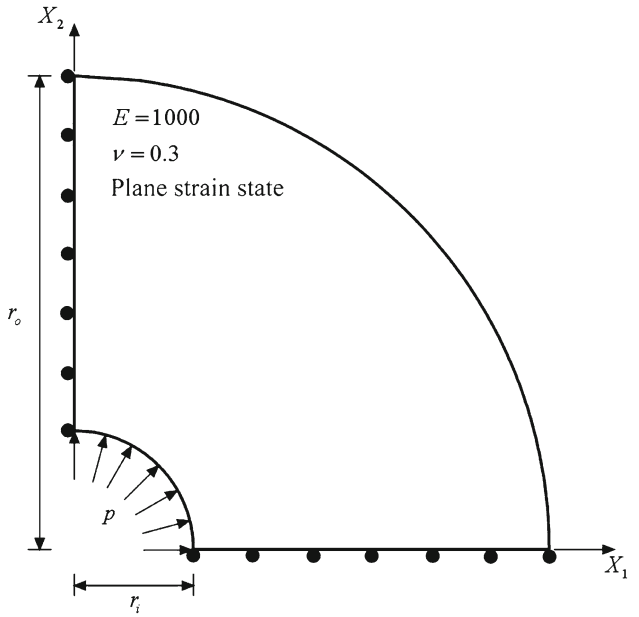

Fig. 6 A quarter model of the thick-walled cylinder under uniform internal pressure

conforming to plane strain condition are given by

$$u_r = \frac{1+\nu}{E}\left[-\frac{A}{r} + 2C\,(1-2\nu)\,r\right], \quad u_\theta = 0 \tag{48}$$

and

$$\sigma_r = \frac{A}{r^2} + 2C, \quad \sigma_\theta = -\frac{A}{r^2} + 2C, \quad \sigma_{r\theta} = 0 \tag{49}$$

where

$$A = -\frac{r_i^2 r_o^2 p}{r_o^2 - r_i^2}, \quad C = \frac{r_i^2 p}{2\left(r_o^2 - r_i^2\right)}$$

Considering the axisymmetric property of the problem, only one quarter of the solution domain is studied (see Fig. 6) and nine 8-node elements shown in Fig. 7 are utilized to model the domain of interest.

In the proposed model, it is important to explore the influence of the position of source points on the accuracy and stability of numerical results. Figs. 8 and 9 show respectively variations of the hoop stress and the condition number of matrix **H** with parameter γ. As expected, it can be seen from these two figures that the results of both stress and condition number are stable within a wide range of parameter γ ($2 < \gamma < 10$). Generally, for the small value of γ($\gamma < 2$), which means that the source points are close to the element boundary, the disturbance of singularity of the fundamental solutions on numerical accuracy may be strong. Conversely, too large γ means that the source points are remote from the element boundary, so that the potential round-off error in floating point arithmetic will produce the matrix **H** with nearly same elements and thus causes a larger

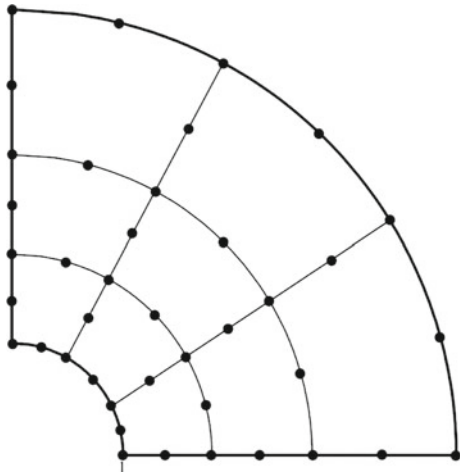

Fig. 7 Configuration of mesh division with nine 8-node elements for both HFS-FEM and ABAQUS

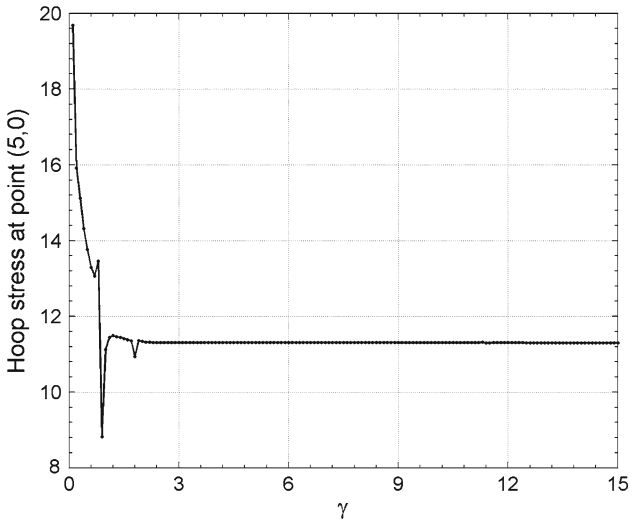

Fig. 8 The variation of hoop stress caused by different γ

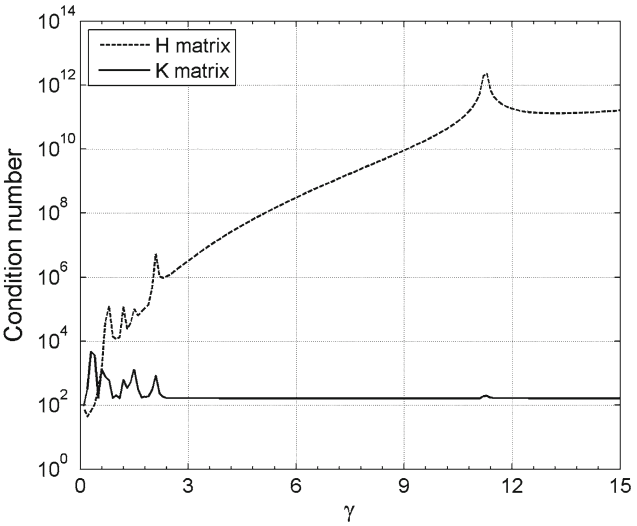

Fig. 9 The variation of condition number caused by different γ

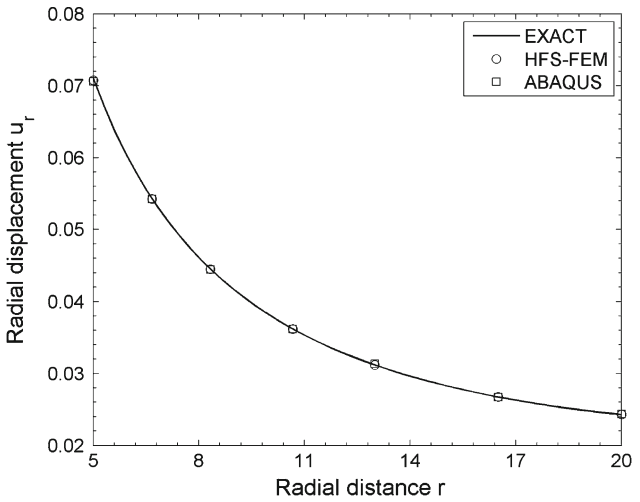

Fig. 10 Radial displacement along the radial direction

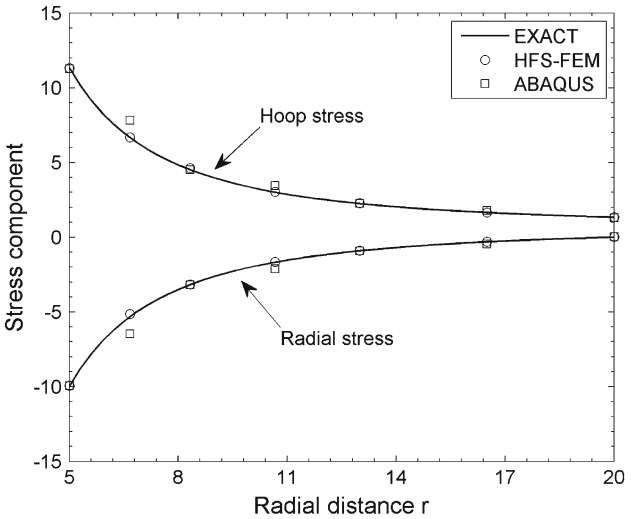

Fig. 11 Hoop and radial stress components along the radial direction

condition number of the **H** matrix, which is disadvantageous to the inverse manipulation of the **H** matrix [30]. Thus, it is suggested to choose parameter γ in the range [2,10]. In the following computation, the parameter γ is chosen to be 4 to produce reliable results. Results for the radial displacement, hoop and radial stress components are plotted in Figs. 10 and 11, respectively, from which we can see that the proposed HFS-FEM and ABAQUS with same mesh provide almost the same displacements along the radial direction, whereas for stress distribution adjacent to the internal boundary there are some discrepancies between the results from the two approaches. It appears that the proposed approach has superior accuracy to that of ABAQUS. Further, to assess the performance of the proposed HFS-FEM relative to HT-FEM, numerical results from both HFS-FEM and HT-FEM are presented in Table 2, in which the results of HT-FEM is obtained with the available codes in Reference [3] and the number of Trefftz functions for each element is taken to be 15. It can be seen from Table 2 that the performance of the HFS-FEM is better than that of the HT-FEM with same mesh density in this example. Finally, to demonstrate the convergence performance of the proposed approach, three different meshes of 4, 9, 16 elements are used for modeling the problem. Fig. 12 displays the convergence behavior of radial displacement and radial and hoop stresses with mesh refinement. The convergent rate is indicated by the normalized error given in Eq. (46). Although Fig. 12 does not show a uniform convergent rate, the error of the results from the proposed formulation decreases along with an increase in the number of nodal DOFs (two DOFs at each node).

Table 2 Numerical comparison of the present HFS-FEM and HT-FEM

	r				
	5.000	6.496	10.394	16.078	20.000
HFS-FEM					
u_r	0.071	0.056	0.037	0.027	0.024
σ_r	−9.930	−5.679	−1.799	−0.366	0.010
σ_θ	11.312	6.975	3.127	1.697	1.342
HT-FEM					
u_r	0.070	0.056	0.037	0.027	0.024
σ_r	−7.076	−5.731	−1.817	−0.372	0.084
σ_θ	8.118	7.059	3.144	1.702	1.231
EXACT					
u_r	0.071	0.056	0.037	0.027	0.024
σ_r	−10.000	−5.652	−1.802	−0.365	0.000
σ_θ	11.333	6.985	3.135	1.698	1.333

5.3 Bimaterial problem

As the third example, we consider a bimaterial problem taking from Ref. [31] as shown in Fig. 13a, subject to the Dirichlet boundary conditions which are applied by the following exact solutions

$$\begin{cases} u_1^{\mathrm{I}} = u_1^{\mathrm{II}} = X_1 \\ u_2^{\mathrm{I}} = u_2^{\mathrm{II}} = X_2 \end{cases} \tag{50}$$

with $E^{\mathrm{I}} = 2.10$, $\nu^{\mathrm{I}} = 0.3$ and $E^{\mathrm{II}} = 2.70$, $\nu^{\mathrm{II}} = 0.1$ for plane stress state. This presents a combination of steel and a higher stiffness material and gives constant stress distributions in each domain, i.e. $\sigma_{11}^i = \sigma_{22}^i = E^i/(1-\nu^i)$ and $\sigma_{12}^i = 0$ for $i = \mathrm{I}, \mathrm{II}$.

To investigate the sensitivity of the proposed formulation to mesh distortion, the solution domain is modeled utilizing 16 8-node elements with a different distortion parameter e (see Fig. 13b). The results displayed in Figs. 14 and 15 show that the presented approach has very good accuracy for the case of a bimaterial problem compared to the available

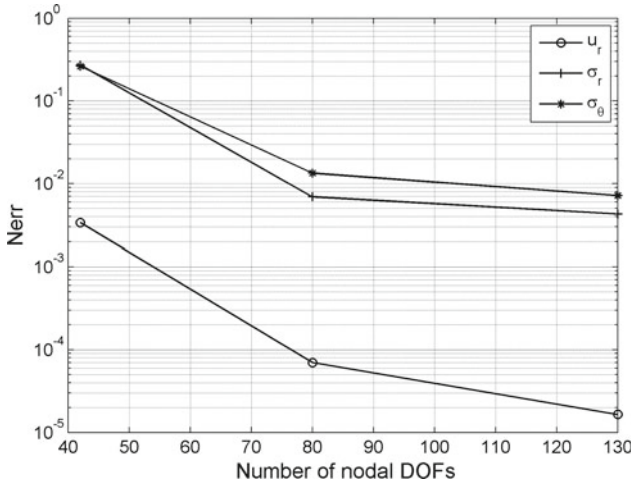

Fig. 12 Convergence demonstration of the presented method

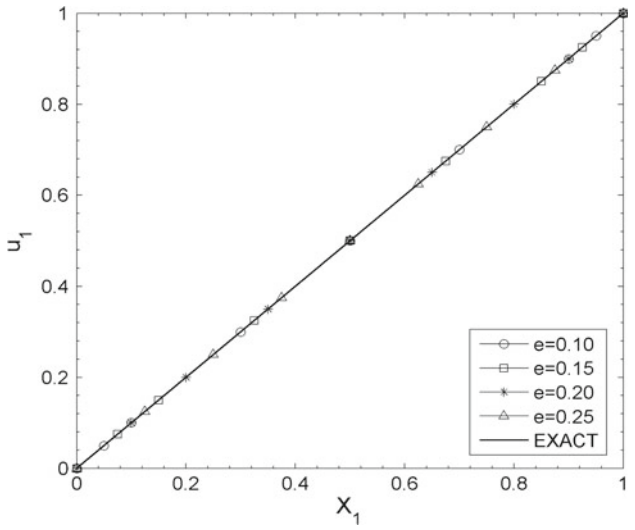

Fig. 14 Displacement variation along the interface for distorted and undistorted hybrid element meshes

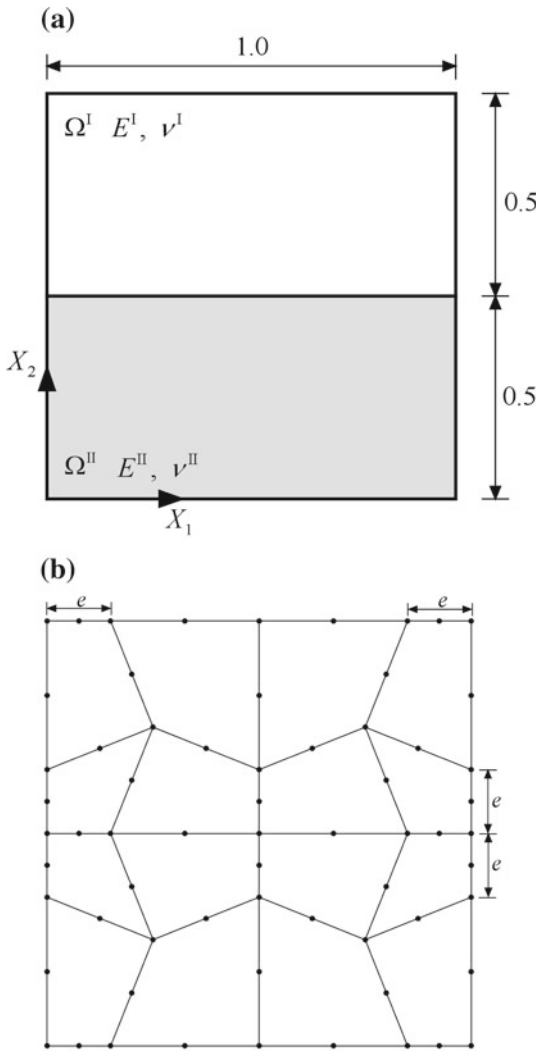

Fig. 13 Illustration of (**a**) bimaterial modeling and (**b**) distorted mesh

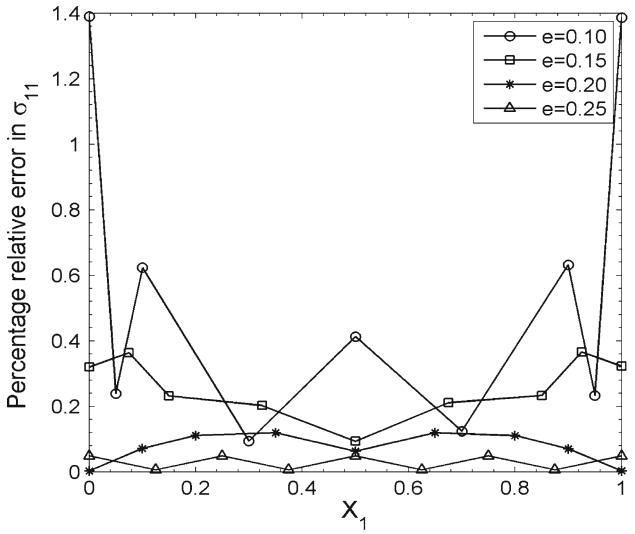

Fig. 15 Stress variation along the interface for distorted and undistorted hybrid element meshes

analytical solutions, and the maximum percentage relative error in stress σ_{11} is just 1.4%, even for highly distorted mesh, that is $e = 0.10$. The proposed hybrid formulation exhibits, therefore, remarkable insensitivity to mesh distortion. Simultaneously, the feasible treatment for multi-material cases is displayed in the solution procedure of the HFS-FEM, compared to other Green's-functions-based methods such as the MFS and BEM, in which extra equations must be supplied to meet the requirement of interface continuity.

5.4 Plate with a circular hole under tension

The stress concentration near a hole is a critical issue for the strength of many engineering structures, and the purpose

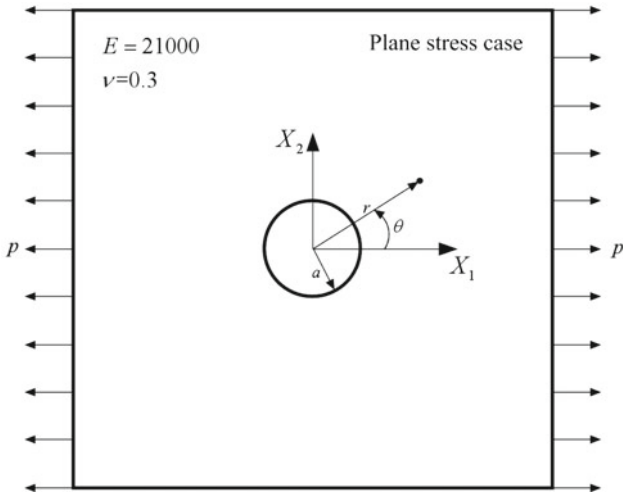

Fig. 16 Square plate with centered circular hole under remote tension

of this example is to illustrate the mesh reduction technique with a specially developed circular hole element in the presented method. Fig. 16 presents a 3 × 3 square plate with a central circular hole subjected to uniaxial uniform tensile load p in the X_1 direction. The rim of the hole is free of forces. In particular, when the outer edges tends to infinity, corresponding analytical solutions are available in the polar coordinate (r, θ) by

$$\begin{cases} \sigma_r = \frac{q}{2}\left(1 - \frac{a^2}{r^2}\right) + \frac{q}{2}\left(1 + \frac{3a^4}{r^4} - \frac{4a^2}{r^2}\right)\cos 2\theta \\ \sigma_\theta = \frac{q}{2}\left(1 + \frac{a^2}{r^2}\right) - \frac{q}{2}\left(1 + \frac{3a^4}{r^4}\right)\cos 2\theta \\ \sigma_{r\theta} = -\frac{q}{2}\left(1 - \frac{3a^4}{r^4} + \frac{2a^2}{r^2}\right)\sin 2\theta \end{cases} \tag{51}$$

from which we can observe that the hoop stress at the upper and lower critical points of the hole is tensile and three times as high as the remote tensile stress, whereas at the left and right ends of the hole the hoop stress is compressive and has a value equal to the remote stress.

To simulate stress concentration on the hole boundary, we first assume that the radius of the hole is $a = 0.4$, and a special element with side length $l = 0.85$ is used in conjunction with 32 conventional elements, as shown in Fig. 17, in the

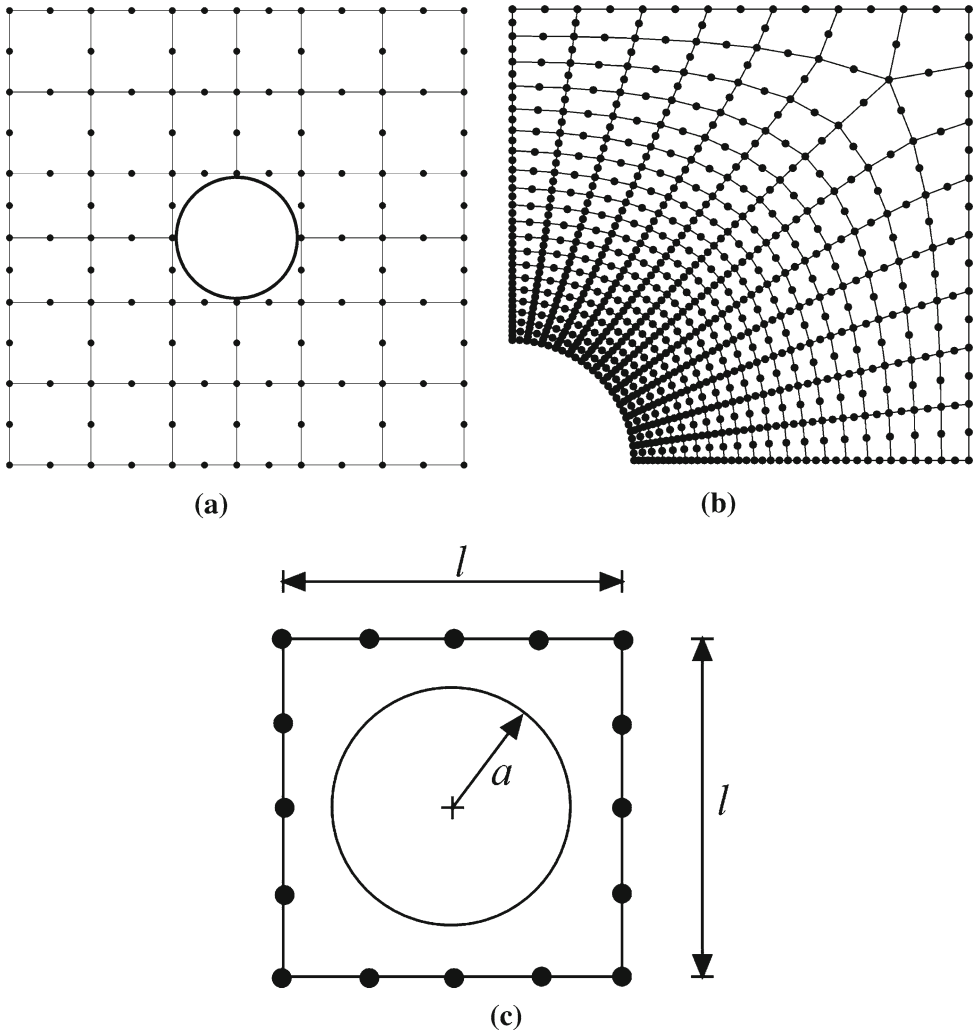

Fig. 17 HFS-FEM mesh (**a**), ABAQUS mesh (**b**), and special circular hole element (**c**)

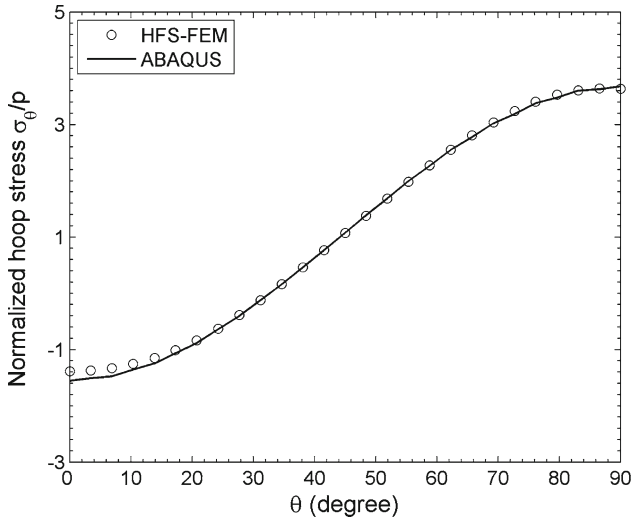

Fig. 18 Variation of hoop stress on the rim of the circular hole

Table 3 Stress concentration factor at the upper point of the hole

Radius a	*Stress concentration factor* $\left(\text{SCF} = \frac{\sigma_\theta}{p}\right)$		*Rerr* (SCF)
	ABAQUS	HFS-FEM	
0.425	3.775	3.575	5.29%
0.400	3.678	3.636	1.14%
0.300	3.358	3.191	4.97%
0.200	3.156	3.131	0.79%
0.100	3.023	3.030	0.23%
0.050	2.978	3.007	0.97%

computation. Plane stress is assumed with $E = 21000$ and $\nu = 0.3$. The hoop stress along the hole boundary is plotted in Fig. 18, in which the results from ABAQUS with 261 8-node quadrilateral elements in a 1/4 model are provided for comparison. It is clear that the results of the proposed approach agree well with those from ABAQUS: the stress concentration factor at the upper point of the hole is 3.633 in HFS-FEM whereas the value is 3.678 in ABAQUS. However, the proposed HFS-FEM uses fewer elements than ABAQUS.

Next, to investigate the effect of the ratio of the radius of the hole to the side length of the plate on the performance of the special circular hole element, we keep the mesh invariable, and solve the problem by changing the radius of the hole. The numerical results for stress concentration at the upper point of the hole are listed in Table 3. Good agreement is observed between the HFS-FEM and ABAQUS, and the maximum relative error is about 5%. This means that a larger element can be used to enclose a circular hole without a dramatic decrease of accuracy. Moreover, it can be seen that as the hole becomes smaller, the maximum stress concentration factor tends to 3.0, which corresponds to the analytical solution (51) in an infinite domain. Numerical results show that the proposed approach can deal with local defects effectively by using proper special fundamental solutions with less meshing effort. Moreover, it can be seen that the adjustment of the radius of circular hole doesn't require the mesh regeneration in the proposed algorithm.

6 Conclusions

Details of the implementation of the proposed fundamental solution-based hybrid finite element formulation with standard elements and special circular hole element were discussed in this paper. As in the fundamental solutions-based method such as boundary element method, all integrals in the present formulation are performed along the element boundary only, instead of in the entire element domain of interest. The hybrid functional developed in the present method enables us to construct arbitrarily shaped elements and guarantee the continuity conditions of fields between adjacent elements. The numerical examples considered demonstrate that the hybrid approach presented can achieve stable results of good accuracy with a relatively small number of elements. The exciting feature of the HFS-FEM, perhaps, is that the use of special elements to model critical regions around a hole is especially effective and can significantly reduce modeling effort and computing cost during analysis. Simultaneously the algorithm can avoid mesh regeneration when the radius of circular hole is changed.

References

1. Pian THH (1964) Derivation of element stiffness matrices by assumed stress distribution. AIAA J 2:1333–1335
2. Qin QH (2000) The Trefftz finite and boundary element method. WIT press, Boston
3. Qin QH, Wang H (2008) Matlab and C programming for Trefftz finite element methods. CRC Press, New York
4. Piltner R (2008) Some remarks on hybrid-Trefftz finite elements with elliptic holes. Finite Elem Anal Des 44:767–772
5. Jirousek J, Venkatesh A (1992) Hybrid-Trefftz plane elasticity elements with p-method capabilities. Int J Numer Meth Eng 35:1443–1472
6. Freitas JAT, Bussamra FLS (2000) Three-dimensional hybrid-Trefftz stress elements. Int J Numer Meth Eng 47:927–950
7. Qin QH (1995) Hybrid Trefftz finite element method for Reissner plates on an elastic foundation. Comput Meth Appl Mech Eng 122:379–392
8. Jirousek J, Wroblewski A, Qin QH, He XQ (1995) A family of quadrilateral hybrid-trefftz p-elements for thick plate analysis. Comput Meth Appl Mech Eng 127:315–344
9. Qin QH (1994) Hybrid Trefftz finite element approach for plate bending on an elastic foundation. Appl Mathe Model 18:334–339
10. Qin QH (1996) Transient plate bending analysis by hybrid Trefftz element approach. Comm Numer Meth Eng 12:609–616
11. Freitas JAT (1997) Hybrid-Trefftz displacement and stress elements for elastodynamic analysis in the frequency domain. Comput Assis Mech Eng Sci 4:345–368

12. Jirousek J, Qin QH (1996) Application of hybrid-Trefftz element approach to transient heat conduction analysis. Comput Struct 58:195–201
13. Qin QH (1995) Postbuckling analysis of thin plates by a hybrid Trefftz finite element method. Comput Meth Appl Mech Eng 128:123–136
14. Qin QH (2005) Formulation of hybrid Trefftz finite element method for elastoplasticity. Appl Mathe Model 29:235–252
15. Leconte N, Langrand B, Markiewicz E (2008) Toward a Hybrid-Trefftz element with a hole for elasto-plasticity? J Comput Appl Math 218:88–95
16. Qin QH (2003) Variational formulations for TFEM of piezoelectricity. Int J Solid Struct 40:6335–6346
17. Wang H, Qin QH, Arounsavat D (2007) Application of hybrid Trefftz finite element method to non-linear problems of minimal surface. Int J Numer Meth Eng 69:1262–1277
18. Wang H, Qin QH (2009) Hybrid FEM with fundamental solutions as trial functions for heat conduction simulation. Acta Mech Solida Sin 22:487–498
19. Wang H, Cao LL, Qin QH (2010) Hybrid graded element model for nonlinear functionallly graded materials. Mech Adv Mater Struct, accepted for publication
20. Wang H, Qin QH (2010) Fundamental-solution-based finite element model for plane orthotropic elastic bodies. Eur J Mech Solid/A 29:801–809
21. Muskhelishvili NI (1963) Some basic problems of the mathematical theory of elasticity, 4th edn. Noordhoff, Netherlands
22. Brebbia CA, Telles JCF, Wrobel LC (1984) Boundary element techniques. Springer-Verlag, Berlin
23. Tang SG, Cao ZY (1998) Complex fundamental solutions for semi-infinite plane and infinite plane with hole under various boundary conditions. Appl Math Mech 19:335–344; (in Chinese)
24. Kupradze VD, Aleksidze MA (1964) The method of functional equations for the approximate solution of certain boundary value problems. USSR Comput Math Math Phys 4:82–126
25. Wang H, Qin QH (2008) Meshless approach for thermo-mechanical analysis of functionally graded materials. Eng Anal Bound Elem 32:704–712
26. Wang H, Qin QH, Kang YL (2006) A meshless model for transient heat conduction in functionally graded materials. Comput Mech 38:51–60
27. Zhang JM, Yao ZH, Tanaka M (2003) The meshless regular hybrid boundary node method for 2D linear elasticity. Eng Anal Bound Elem 27:259–268
28. Sze KY, Liu GH, Fan H (2010) Four- and eight-node hybrid-Trefftz quadrilateral finite element models for helmholtz problem. Comput Meth Appl Mech Eng 199:598–614
29. Simpson H, Spector S (1987) On the positivity of the second variation in finite elasticity. Arch Ration Mech Anal 98:1–30
30. Mitic P, Rashed YF (2004) Convergence and stability of the method of meshless fundamental solutions using an array of randomly distributed sources. Eng Anal Bound Elem 28:143–153
31. Berger JR, Karageorghis A (2001) The method of fundamental solutions for layered elastic materials. Eng Anal Bound Elem 25:877–886